ADVANCED MATERIALS TECHNOLOGIES
www.advmattechnol.de

Multielement Polychromatic 2D Liquid Crystal Dammann Gratings

*Zimo Zhao, Bohan Chen, Patrick S. Salter, Martin J. Booth, Dominic O'Brien, Steve J. Elston, and Stephen M. Morris**

Multielement and multiwavelength switchable Dammann gratings are demonstrated in polymerizable nematic liquid crystal (LC) devices fabricated using two-photon polymerization direct laser writing. To begin with, a single element 2D Dammann grating, with a diffraction efficiency of around 60%, is fabricated in a thin polymerizable LC layer such that the grating could be activated and deactivated with the application and removal of an external applied voltage. The impact of the fabrication parameters on the resulting intensity distribution in the far-field diffraction pattern is presented and discussed, along with results for the response times, which are found to be less than that recorded for the regions of the LC device that did not consist of the laser-written grating. A multielement device is then presented that exhibits two different Dammann gratings that are activated by the application of two different voltage amplitudes. Results for the corresponding far-field intensity profiles and response times are presented, which demonstrate that high quality laser written switchable Dammann gratings can be fabricated in polymerizable LCs. These switchable elements have potential in programmable beam shaping, microscopy and optical communication devices.

1. Introduction

A Dammann grating is a beamlet array generator which efficiently converts a monochromatic incident beam into a finite array of spots with a uniform intensity distribution.[1–7] The original design of the grating was put forward by Dammann in 1977, when a binary-phase $(0, \pi)$ grating structure was proposed that could generate an array of multiple beams in the Fourier plane.[1,2] Compared with conventional gratings, which consist of narrow grooves separated by a fixed period, Dammann gratings consist of features of specific lengths that can generate beamlets of different configurations in the far field. Dammann's method of generating beams with uniformly distributed intensity is attractive for three reasons. First, it is based on modifying the phase information of the incident light without changing the intensity distribution, which allows for a high throughput of light. Second, these gratings are binary, which means that they can be fabricated with techniques such as photolithography, ion etching or laser writing. Third, since a Dammann grating can split the incident beam into a uniform array, it can be combined with other more advanced patterns to modify multiple beams simultaneously into desired beam shapes and profiles.

Since the first demonstration, and with the development of microfabrication technologies,[8–11] Dammann gratings have been successfully fabricated in a range of different materials and for various technological applications.[7,12–15] The initial pattern design method proposed by Dammann was for a symmetric grating that was targeted for the generation of an odd number of spots along one dimension. The nonsymmetric pattern design was first proposed by Mait in 1988 to generate a pattern consisting of an even number of spots[5]. Later, Morrison reduced the computational complexity of the process that is required to generate the pattern parameters by utilizing a symmetric phase shift profile, which led to the generation of an even number of spots in the far-field.[16] Alternatively, a grating with a nonorthogonal two-dimensional pattern was proposed by Vasara[17] in order to develop arrays with more irregular configurations.[14] A group of numerical solutions for Dammann gratings from 2 to 64 was computed and presented by Zhou[18] and was later employed for a number of different Dammann grating designs including circular Dammann gratings,[19] three-dimensional Dammann gratings,[20] and a beam shaping device.[13] In terms of technological applications, Dammann gratings have been widely applied to the fields of optical communications,[21] optical computing,[22,23] and laser beam shaping.[4,13,24]

A common method for fabricating Dammann gratings is to use ultraviolet (UV) lithography with high-resolution binary phase masks to form the required pattern on a fused silica substrate. This method, in general, can produce high quality Dammann gratings with fabrication errors less than 2%.[14,25] There have also been a number of attempts to fabricate Dammann gratings in various liquid crystal (LC) materials and

Z. Zhao, B. Chen, P. S. Salter, M. J. Booth, D. O'Brien, S. J. Elston, S. M. Morris
Department of Engineering Science
University of Oxford
Parks Road, Oxford OX1 3PJ, UK
E-mail: stephen.morris@eng.ox.ac.uk

The ORCID identification number(s) for the author(s) of this article can be found under https://doi.org/10.1002/admt.202200861.

DOI: 10.1002/admt.202200861

devices.[26–30] To create different phase profiles within LC materials, the spatial orientations of the director (the average pointing direction of the molecules) should be precisely controlled. Toward this end, photoalignment materials have been used to functionalize the surface of a substrate so as to align the LC director along a desired direction,[18,19] and this has been a popular approach for the fabrication of Dammann gratings in LC devices.[26,29–32] In this case, the sulfonic azobenzene dye, SD1, which is a photoalignment material is the surface alignment material of choice that is employed in the literature.[26,29–32]

There are, however, significant limitations when using photoalignment layers of this type, such as the perishable nature of the alignment layer after a relatively short period of time. Moreover, because the orientation of the LC director is determined by the static alignment pattern on the surface, it is therefore difficult to generate complex three-dimensional structures using this method. Meanwhile, to fabricate Dammann gratings with photoalignment layers, predesigned photomasks are often required, which restricts the flexibility of the pattern design. Furthermore, even though electrical tunability of an LC Dammann grating has been reported by Wang et al.,[29] the Dammann grating pattern reported was still based on surface photoalignment layers that were patterned with photomasks. In this case, the application of an external electric field resulted in overcoming the surface alignment effects so as to reorient the LC director and switch the Dammann pattern on and off. Here the whole structure was limited to a surface-induced alignment rather than a bulk 3D configuration. Furthermore, these Dammann gratings are often designed for operation at a single specific wavelength rather than a range of wavelengths.

In this paper, bi-element switchable Dammann gratings are reported that can operate at multiple wavelengths by tuning the applied voltage. These switchable gratings have been fabricated in polymerizable LC resins using two-photon polymerization direct laser writing (TPP-DLW). This approach negates the need for perishable photoalignment layers or static configurations; it also enables more than one grating to be encoded into the LC layer at any one time. As shown previously, TPP-DLW allows for the fabrication of sophisticated 3-dimentional microstructures in the polymerizable LC resin by locking-in the orientation of the LC director inside the network at the moment of exposure to the laser writer.[33–36] Using this approach, we have been able to demonstrate switch diffractive optic elements.[36] Here we report the fabrication and characterization of both a single element switchable 2-D Dammann grating and multielement interchangeable 2-D Dammann gratings written into a region of LC covering a size of 1024 μm × 1024 μm. Simulations are conducted before fabrication to determine the optimum fabrication parameters that result in voxels with dimensions of ≈1 μm radius and ≈8 μm in length. Previous research has shown that there is a strong correlation between the predicted voxel dimensions and the resulting polymerized structures, as evidenced by scanning electron microscope (SEM) images.[34] This is followed by the presentation of experimental results of the intensity distribution across the array in the far-field, the response times for either switching the gratings on and off or switching between gratings, and the diffraction efficiency. It is shown that a relatively uniform intensity distribution is demonstrated for the interchangeable diffraction patterns, which highlights the potential of these switchable laser-written LC Dammann gratings. Moreover, by adjusting the voltage applied to turn on the grating, these switchable Dammann gratings can be made to function across a range of different wavelengths.

Figure 1 illustrates the concept of fabricating a single layer Dammann grating in a LC device with TPP-DLW along with the corresponding diffraction images observed in the replay field when the grating is activated or deactivated. Figure 1a demonstrates the process of laser writing into an LC device. The alignment of the LC director is first controlled by external electric field, and then locked by polymer networks using director laser writing. The writing process of locked and tunable regions of a Dammann grating using two-photon laser is illustrated in Figure 1b. After the fabrication of a Dammann grating, external electric fields are applied again to activate and deactivate the pattern in the replay field and the expected results are shown in Figures 1c and d.

2. Dammann Grating Design

The design of the Dammann gratings used in this study was based on scalar diffraction theory.[1,2,4] It is assumed that the grating is illuminated by a collimated laser beam with a planar wave front and the output pattern is captured in the far-field. The designed 2D Dammann grating can be represented as a transparency function $g(x, y)$ and the diffraction pattern is represented mathematically by the Fourier transform of the 2-D Dammann grating as $G(u, v)$.

The transparency function $g(x, y)$ can be represented by the product of two individual 1-D grating functions in the x- and y-directions: $g(x, y) = g_1(x)g_2(y)$. For this situation, the Fourier transform of $g(x, y)$ is separable into two directions: $G(u, v) = G_1(u)G_2(v)$, where $G_1(u)$ and $G_2(v)$ are the 1-D Fourier transform of $g_1(x)$ and $g_2(y)$, respectively. The grating structures in the x-direction ($g_1(x)$) and y-direction ($g_2(y)$) do not necessarily need to be the same, as the number of spots in the diffraction pattern in either direction can be different. However, for simplicity, let's assume $g_1(x) = g_2(y) = g(\xi)$ and $G_1(u) = G_2(v) = G(u)$. Then the main computational problem becomes finding the transparency function $g(\xi)$ with phase-only form: $g(\xi) = e^{-i\phi(\xi)}$ and its Fourier transform will then generate $G(u)$.

In order to reduce the computational complexity and increase usability, the phase difference $\phi(\xi)$ introduced by the grating was restricted to be 0 and π only. So, for the grating, the value of $g(\xi)$ was restricted to be $g(\xi) = 1$ and $g(\xi) = -1$ only. Furthermore, in order to generate a diffraction pattern, the grating should be a periodic pattern, thus $g(\xi) = g(\xi + \Delta\xi)$. For the original design proposed by Dammann,[2] the grating was an even function, which will generate an odd number of spots in the 1-D diffraction pattern. However, Killat[3] and Mait[5] also proposed using a nonsymmetric design of the gratings, which is an odd function, and its 1-D diffraction pattern therefore contains an even number of spots in the array. For our analysis, it is convenient to set $\Delta\xi = 1$ as a way of normalizing the results. Because the grating can be either even or odd, the transition points in the negative half period is then the mirror of that in the positive half period. Thus, the only free parameters for

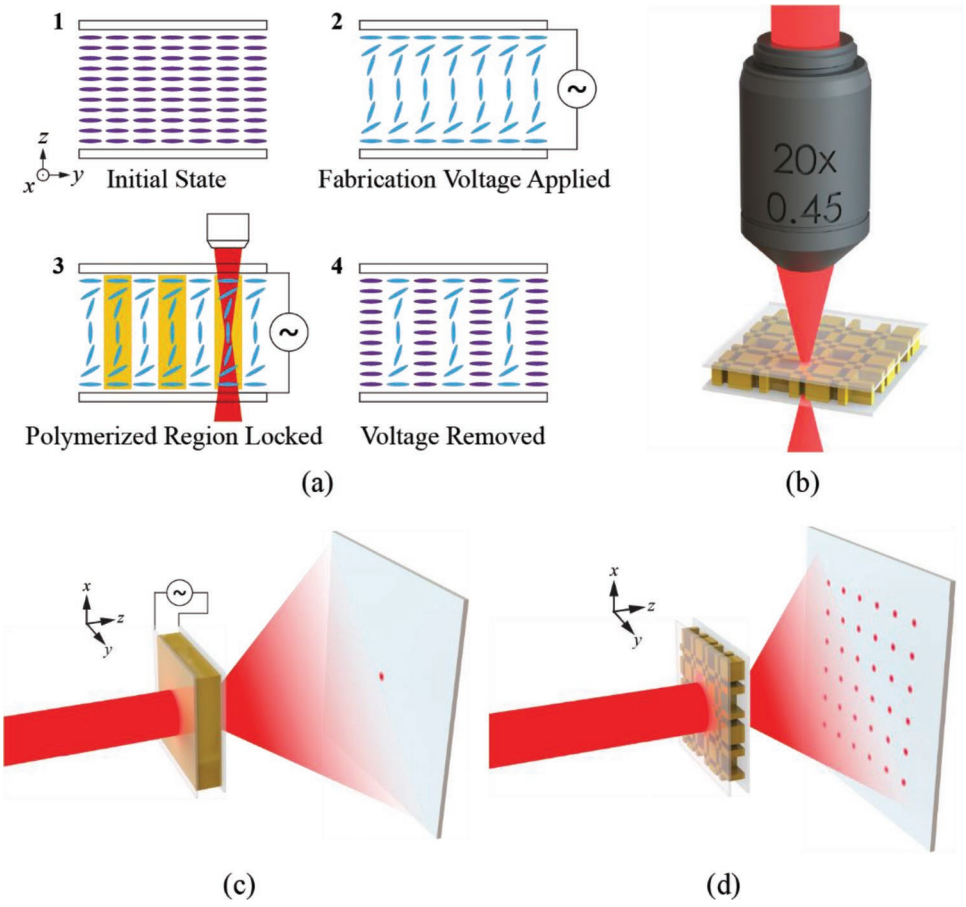

Figure 1. Illustration of the concept of an electrically switchable liquid crystal (LC) Dammann grating fabricated using two-photon polymerization direct laser writing. a) The process of laser writing into an LC device with an electric field to control the alignment of the LC director. b) Illustration of a laser written Dammann grating in an LC device. c) Illustration of the replay field when the LC device is not activated when the fabrication voltage is applied. d) Illustration of the replay field when the Dammann grating is activated with no voltage applied.

either of the structures are the positive transition points ξ_1, ξ_2, ξ_3, ⋯, ξ_N in the interval $0 < \xi \le 0.5$.

The next goal is to compute the transition points ξ_1, ξ_2, ξ_3, ⋯, ξ_N so that the zeroth (only for the odd grating) and $\pm 1^{st}$, ⋯, $\pm N^{th}$ diffraction orders have equal intensities. The number of transition points N relates to the number of spots in the array. For an even symmetric grating, it will generate $2N + 1$ spots in the 1D diffraction pattern. For an odd nonsymmetric grating, it will generate $2N$ spots in the 1D diffraction pattern. In the following discussion, we use the boundary conditions $\xi_0 = 0$ and $\xi_{N+1} = 0.5$.

For an even symmetric grating,[2] the transparency function $g_e(\xi)$ is written as

$$g_e(\xi) = \begin{cases} \sum_{n=0}^{N} (-1)^n \operatorname{rect}\left[\dfrac{\xi - (\xi_{n+1} + \xi_n)/2}{\xi_{n+1} - \xi_n}\right], 0 < \xi \le 0.5 \\ \sum_{n=0}^{N} (-1)^n \operatorname{rect}\left[\dfrac{\xi + (\xi_{n+1} + \xi_n)/2}{\xi_n - \xi_{n+1}}\right], -0.5 \le \xi < 0 \end{cases} \quad (1)$$

By applying the Fourier transform to Equation (1), the odd-numbered diffraction orders in the Fourier plane are then expressed as

$$G_e(u) = \mathcal{F}\{g_e(\xi)\} = \begin{cases} \dfrac{1}{u\pi} \sum_{n=0}^{N} (-1)^n \left(\sin 2\pi u \xi_{n+1} - \sin 2\pi u \xi_n\right), u \ne 0 \\ 2\sum_{n=0}^{N} (-1)^n (\xi_{n+1} - \xi_n), u = 0 \end{cases} \quad (2)$$

Alternatively, for the odd nonsymmetric grating,[5] the transparency function $g_o(\xi)$ takes the form

$$g_o(\xi) = \begin{cases} \sum_{n=0}^{N} (-1)^n \operatorname{rect}\left[\dfrac{\xi - (\xi_{n+1} + \xi_n)/2}{\xi_{n+1} - \xi_n}\right], 0 < \xi \le 0.5 \\ -\sum_{n=0}^{N} (-1)^n \operatorname{rect}\left[\dfrac{\xi + (\xi_{n+1} + \xi_n)/2}{\xi_n - \xi_{n+1}}\right], -0.5 \le \xi < 0 \end{cases} \quad (3)$$

In the same way, by applying the Fourier transform to Equation 3, it is straightforward to derive similar results for the even-numbered diffraction orders in the Fourier plane, which take the form

$$G_o(u) = \mathcal{F}\{g_o(\xi)\} = \begin{cases} \dfrac{1}{u\pi i} \sum_{n=0}^{N} (-1)^n \left(\cos 2\pi u \xi_{n+1} - \cos 2\pi u \xi_n\right), u \ne 0 \\ 0, u = 0 \end{cases} \quad (4)$$

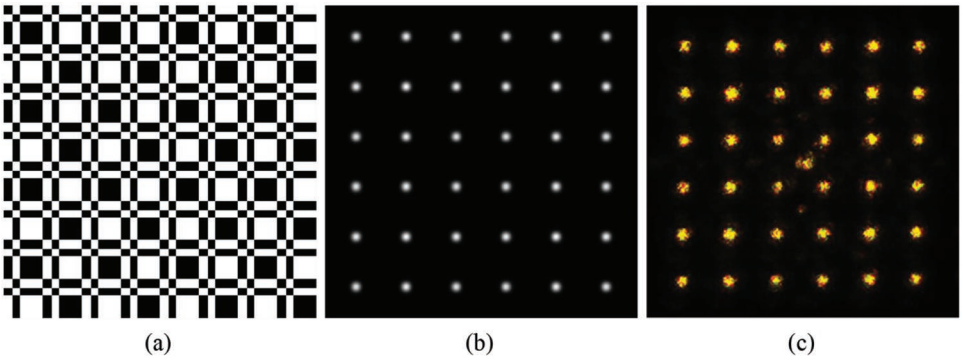

Figure 2. Design, simulation, and experimental characterization (using a spatial light modulator) of a 2D Dammann grating. a) Configuration of a Dammann grating that gives rise to a square array of 6 × 6 spots in the replay field. b) Simulation of the corresponding replay field pattern. c) Photograph of the replay field pattern observed when the Dammann grating in (a) was loaded onto a spatial light modulator.

The above expressions also highlight why the symmetric grating leads to an odd number of diffraction spots while the nonsymmetric grating leads to an even number of diffraction spots in the far-field. According to Parseval's theorem, the sum of the intensities of all diffraction orders is 1: $\sum_{u=-\infty}^{\infty} I_u = \sum_{u=-\infty}^{\infty} |G(u)|^2 = 1$. Thus, for the design of the gratings, a group of solutions for the transition points $\xi = [\xi_1, \xi_2, \xi_3, \cdots, \xi_N]$ is required to create an array of diffraction spots with uniform intensity distribution, where $I_0(\xi) = I_{\pm1}(\xi) = \cdots = I_{\pm N}(\xi)$. Numerical approaches are utilized to derive solutions for ξ, and Zhou and Liu[18] have provided a detailed table of the transition points required for generating an array of any desired size. For all of the experiments reported in this paper, the transition points used in the pattern design have been taken from their results. The transition point values for the 6 × 6-grating used in this paper were: $\xi_1 = 0.11444$ and $\xi_2 = 0.20897$. An example of a 6 × 6 grating design based on these transition points ξ_1 and ξ_2 is shown in **Figure 2**a.

In the real device, the transition points are quantized by the fabrication process, which used a 1 µm square region to define each pixel in the designed pattern. Thus, the pixel numbers of the pattern will affect the quantization error introduced to the transition points from mathematical calculations, and the actual phase change due to the fabrications at the transition point will affect the pattern quality. In order to gain more insight in terms of the factors that influence the actual device performance, simulations were first carried out to determine the optimum design parameters (and consequently the fabrication parameters) that would generate an array of spots with a high diffraction efficiency and a uniform intensity distribution.

3. Simulations of the Far-Field Intensity Distribution of the Dammann Gratings

The diffraction pattern in the far-field can be derived by taking the Fourier transform of the complex light distribution immediately after the grating. By building up a simulation model in MATLAB, the propagating laser beam was modeled using a monochromatic Gaussian beam intensity profile expressed as

$$I(\rho,z) = \frac{I(0,0)}{1+\frac{z^2}{z_R^2}} e^{\frac{-2\rho^2}{w^2}} \tag{5}$$

where $\rho = \sqrt{x^2+y^2}$ is the distance away from the centre of the laser beam; z is the distance away from the waist point of the laser beam; $z_R = \frac{\pi w_0^2}{\lambda}$ is Rayleigh length; and w is the waist size of the laser beam, which is a function of z. By normalising $I(0, 0)$ to 1 for simplification, then Equation (5) at $z = 0$ can be simplified as

$$I(x,y) = e^{\frac{-2(x^2+y^2)}{w_0^2}} \tag{6}$$

where (x, y) is the position in a plane perpendicular to the propagation that is relative to the central position of the beam where maximum intensity is observed. A Dammann grating that gave rise to an array of 6 × 6 spots in the replay(far)-field was then generated by employing the transition point values provided by Zhou.[18] The total pattern size and the grating period were determined first according to the fabrication speed of our DLW system, which was 100 µm per second for a single photo-polymerized line. Each pixel of the design pattern corresponded to a 1 µm square region in the actual device fabricated with the DLW system, which had to be taken into consideration, along with the spot size of the illumination source in the experimental system used to characterize the diffraction patterns. Value 1 of the pixel represents the phase π and value 0 of the pixel represents the phase 0, whose distributions are controlled by the designed transition points. After generating a 1D grating, the 2D pattern was then generated by XOR-ing two 1D gratings with one of them being rotated by 90°. The entire process sequence as well as the simulated Gaussian beam is presented in Figure S1 (Supporting Information).

The final replay image could be derived from the Fourier transform of $S(x, y) = I(x, y) \cdot g(x, y)$. Figure 2a,b illustrates the grating pattern and simulation results of the corresponding replay image in the Fourier plane, respectively. The initial simulation results indicate that the designed Dammann grating pattern creates an array of spots in the replay field as intended

(Figure 2b). However, from the initial simulation results, it was also found that the intensity of the spots was not the same, as expected. To further investigate this, some of the design parameters were adjusted to determine the optimum values.

The first parameter that was tuned was the number of pixels on the designed pattern used to represent the width of one period, as each pixel on the pattern will be interpolated into a 1 μm square in the actual fabrication. By simulating gratings with pixel widths of a single fixed grating period from 16 pixels to 2048 pixels in a pattern with a total size of 8192 × 8192 pixels, and by calculating the maximum variation of the normalized spot intensity, the quality of the gratings (in terms of the intensity distribution in the replay field) can be determined. The values for the transition points were calculated based on the continuity of the axis, which means that the transition point can be any real number in a period. However, for the actual fabrication, it would be very time-consuming to fabricate at the exact transition points. To increase the speed of the fabrication process, but maintain the quality of the gratings, the period was quantized using "pixels," where each pixel corresponds to the minimum spot size of 1 μm in diameter fabricated with the DLW system. One period of the grating can be represented using different numbers of pixels on the pattern image (thus results in different lengths in the actual fabrication), and the transition points were converted and rounded to the nearest integer number of pixels i.e., no half-integer number of pixels.

When the width was small (i.e., 16 pixels), the normalized intensity difference ΔI between the maximum and minimum intensity was $\Delta I|_{T=16} = 0.76$, which indicates a pattern with a significant nonuniform intensity distribution and mismatches with the design target of a uniform Dammann array. For a slightly larger width, i.e., 32 pixels or 64 pixels, the intensity difference becomes $\Delta I|_{T=32} = 0.26$ or $\Delta I|_{T=64} = 0.24$, respectively, which were also not in accord with the initial design. When the period was larger than or equal to 128 pixels, the difference drops to $\Delta I|_{T=128} = 0.06$, which means that the grating period with more than 128 pixels can generate a uniform intensity array with only a small degree of nonuniformity that was less than 0.06 in the Fourier plane. However, when the grating period becomes larger, the gap between each spot in the diffraction pattern will become narrower, which makes it difficult to observe the diffraction pattern on a screen in the replay field. In order to balance the need for low nonuniformity in the intensity distribution of the spots with the size of the diffraction pattern in the replay field, a pixel width of 128 pixels for the period was selected as the fabrication parameter. The normalized intensity difference ΔI between the maximum and minimum intensity for different grating periods are listed in Table S1 (Supporting Information).

The distribution of the intensity and the overall quality of the diffraction pattern was affected by the phase ramp at the transition points between two adjacent pixels with different phase profiles. The ramp represents the gradual phase transition from one pixel to another pixel around the transition point. For the actual fabrication, it is impossible to make the phase change so abrupt at the transition point that there is no ramp in the phase, which reduces the accuracy of the actual fabricated pattern compared with the 'ideal grating', which has a perfect discontinuous phase change at the transition points. To simulate what is observed in practice, and to determine the tolerance in the fabrication, the pattern was intentionally blurred with different averaging kernels (Figure S2, Supporting Information). The Fourier transform of the blurred gratings in Figure S2 (Supporting Information) indicate that if there is a slight blurring of the pattern edge this will not affect the quality of the diffraction spots significantly, while the 0^{th} order will quickly become dominant if the quality of the fabrication of the edges is poor.

Before writing the gratings directly into the LC glass cells, the gratings were characterized experimentally using a spatial light modulator (SLM). The pattern loaded onto the SLM was essentially the same as that presented in Figure 2a but adjusted to utilize the full tunable range and resolution of SLM. The 24-bit RGB image, where 8 green bits are the most significant bits and 8 blue bits are the least significant bits, was loaded into the 16-bit DVI system of the SLM. According to the datasheet of the SLM, the last 8 blue bits are ignored and only an image composed of 8 green bits and 8 red bits will result in a tunable linear output phase of the SLM across the full 16-bit range. From the SLM results presented in Figure 2c, it can be seen that the pattern observed in the replay field agrees well with the design.

The simulations provide detailed guidance about how to choose the most appropriate parameters for the design of the grating and the fabrication of the grating in the LC device to obtain the best quality in terms of the diffraction pattern. The final parameters chosen for this study were as follows: 1) The grating image size was set to 1024 pixels × 1024 pixels, with a grating period width of 128 pixels; 2) the writing speed and power were carefully selected during the fabrication as well to minimize the blurring of the edges of the grating pattern. These fabrication parameters were further verified using the SLM, where a similar environment close to the actual laser-written LC devices is provided.

4. A Switchable 2D Dammann Grating

For this study, the polymerizable nematic LC mixture (IR819-RM257-E7) was used. This was capillary filled into a glass cell with antiparallel rubbed polyimide alignment layers, indium tin oxide electrodes, and a cell gap of 5 μm. **Figure 3** shows the experimental results for a Dammann grating laser written into the polymerizable nematic LC. The size of the grating was set to 512 pixels by 512 pixels where each pixel was fabricated with 2 × 2 1 μm laser-written spots and the number of pixels used to represent each period in the pattern is 128. This results in a grating size of 1024 μm × 1024 μm, which is the same configuration as that used for the testing with the SLM, but with a total pattern size that is scaled by 2. The grating pattern was fabricated for the case when no voltage was applied during fabrication and the target pattern fabricated was designed to exhibit a square array of 6 × 6 spots in the replay-field. Figure 3a shows a polarizing optical microscope (POM) image of the laser written pattern. As the pattern was written at $V_{\text{Fabrication}} = 0.0\ V_{\text{rms}}$, the features are barely visible because of the uniformity in the director field. This is because the laser writing has locked-in the alignment

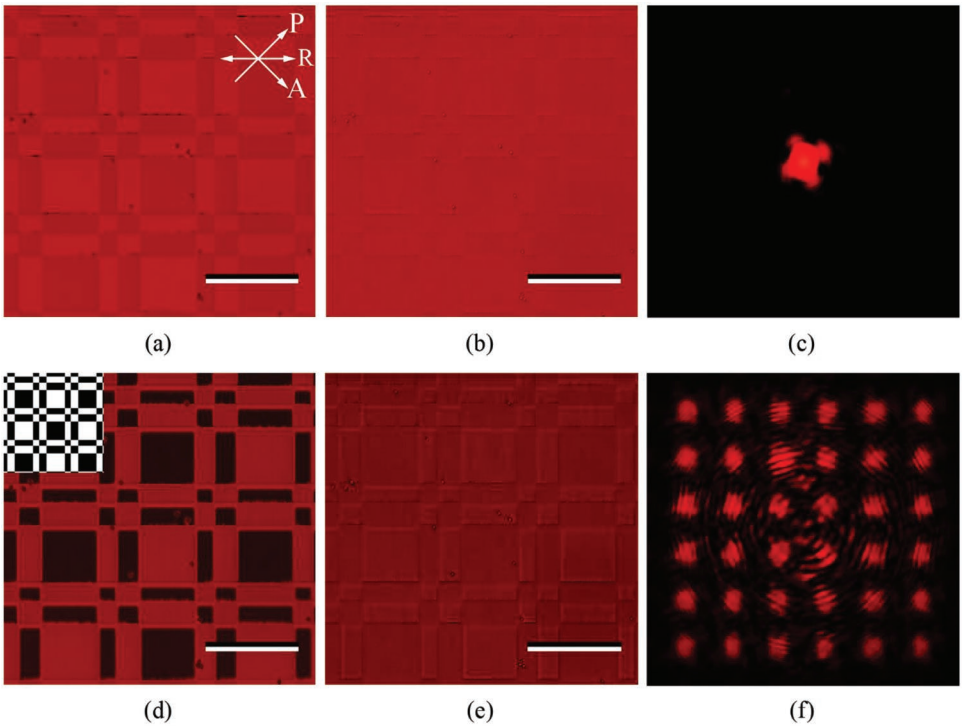

Figure 3. Demonstration of a switchable laser written LC Dammann grating. a) Polarizing Optical Microscope (POM) image of the Dammann grating under the wavelength of 660 nm that gives rise to a 6 × 6 array of spots in the replay field when activated. The POM shows the case for the voltage off-state at $V = 0$ V_{rms}. The scale bar is 120 µm. The arrows indicate the directions of the polarizer (P), analyzer (A), and rubbing direction (R). b) Microscope image of the 6 × 6 square grating with no analyser in the voltage off-state at $V = 0$ V_{rms}. The scale bar is 120 µm. c) Corresponding replay field pattern for the voltage off-state. d) Microscope image of the 6 × 6 square grating in the voltage on-state at $V = 1.3$ V_{rms} (with grating design included in the top left corner). The scale bar represents a length of 120 µm. e) Phase only microscope image of the 6 × 6 square grating with no analyzer in the voltage on-state at $V = 1.3$ V_{rms}. The scale bar indicates 120 µm. f) Corresponding replay field pattern for the voltage on-state at $V = 1.3$ V_{rms}.

at 0.0 V_{rms} for the regions that define the grating. When the device is inspected without an applied field, the director is aligned in the same direction uniformly throughout the sample. Some of the features of the grating can be just made out in the image, and it is believed that this is due to a slight mismatch in the refractive indices between the polymerized and nonpolymerized regions, where the electric field of the laser during the writing process introduced a slight disturbance to the LC director alignments. Figure 3b shows a POM image of the pattern with no analyzer installed to highlight the phase only information from the pattern (which is null here). The features are nearly invisible because the pattern was written at 0.0 V_{rms} where the phase profile is uniform as the director is aligned throughout. When no voltage is applied the grating is inactive and therefore no pattern is generated in the replay field as can be seen in Figure 3c.

To activate the grating and obtain a diffraction pattern, a replay voltage of V_{Replay} = 1.3 V_{rms}, which will provide the pattern with π phase difference at wavelength of 630 nm laser illumination, was applied where it can be seen that a clear Dammann grating appears in the LC device (as is evident from the POM image in Figure 3d). This voltage was selected based on the transmission-voltage curve measured for the sample. It can also be seen in Figure 3d that the fabrication has been successful by comparing the fabricated pattern in the LC cell with the designed pattern (shown as an inset). Phase information was inferred from the POM images with no analyzer installed in the microscope (Figure 3e) by checking the edges of the feature where the regions with different phase profiles are clearly revealed. The director locked-in at 0.0 V_{rms} remains unchanged while the director in the nonlaser written regions are reoriented by the replay voltage 1.3 V_{rms} to create a different phase profile. The mismatch in the refractive indices at the transition edges between the two regions results in the appearance of the grating.

Figure 3f shows the 6 × 6 array of spots generated in the replay field (far field) when the LC device was switched on with a voltage of 1.3 V_{rms}, which demonstrates that the intensity is relatively uniformly distributed amongst the spots. The results show that the fabricated single layer element can readily switch between the two states with no remains of another when at targets voltages. The results also show that the diffracted spots are distributed with a uniform intensity distribution when the grating is activated and completely disappear when the grating is deactivated. Note that the faint concentric circles that can be seen in the image are the result of contributions from other planar optical elements in our 630 nm replay imaging system, such as a ND filter, a half-wave plate and a polarizer. When the voltage applied to the LC is neither 0 V_{rms} nor 1.3 V_{rms}, which are the designed replay voltages, the diffraction pattern will no longer be a uniform beamlet array or simply a nondiffracted spot. Instead, the 0th order spot will become dominant in the

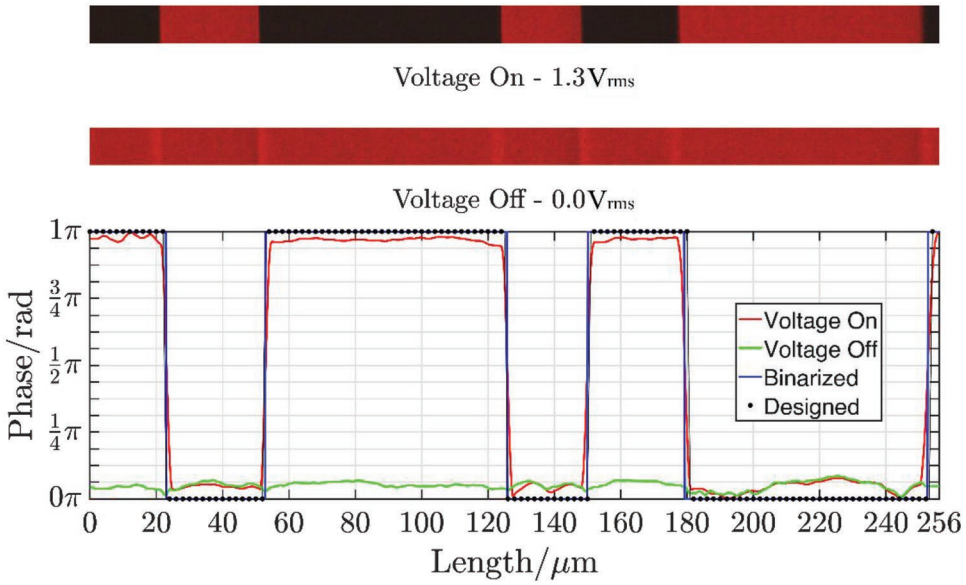

Figure 4. The phase extracted from a cross-section of one period of the grating along the longitudinal direction in the Dammann grating. This grating generates an array of 6 × 6 spots in the replay field. Corresponding microscope images of one period under crossed polarizers (with and without a voltage) for the same length scale are presented above the plot.

replay field with the addition of a beamlet array that is much weaker in intensity. An example of the diffraction pattern recorded in the replay field when 1.0 V_{rms} was applied is illustrated in Figure S3 (Supporting Information).

To analyses the fabrication quality in more detail, the phases for the cross-sections of one grating period for the on and off states were extracted from the POM image and the results are illustrated in **Figure 4**. In the figure, the additional phases introduced by LC birefringence under the voltage activating the pattern are binarized at the threshold, which is half the value between the maximum and minimum phase differences. The actual transition points were then derived from the binarized values. Compared with the designed transition points, which are : $\xi_1 = 0.11444$ and $\xi_2 = 0.20897$ respect to the unit period length 1, the fabricated devices exhibits a deviation $\Delta\xi$ in the transition point of less than 0.02 with respect to the unit period length or less than 2% with respect to the actual fabrication length, which is close to the fabrication quality of UV lithography.[14,15] Direct inspection of the transition points using SEM imaging might be possible. However, due to the process of washing out the nonreacted LC mixture and coating the network for SEM imaging, there will inevitably be some degradation of the polymer network, which could lead to an incorrect interpretation of the transition points.

The rise (10–90%) and fall (90–10%) response times for the switchable grating written into this LC sample with a 5 µm cell gap were found to be of the order of 40 and 200 ms, respectively, which is significantly less than the response times recorded for the nonpolymerized regions of the device, where the response times of the order of 100 and 400 ms were recorded. The switching time measured for the nonpolymerized regions is consistent with the dynamics of the Freedericksz transition[37] and is consistent with observations that the relaxation time is shorter for polymerized nematic LCs compared to the nonpolymerized regions.[38,39]

The efficiency, which is defined as the ratio between the summation of the intensity of all desired 6 × 6 diffraction spots and the nondiffracted initial laser spot, is found to be ≈60%. Figure S4 (Supporting Information) presents the results for the diffraction efficiency as a function of voltage, which describes how much light goes into the 6 × 6 array of spots when the grating is activated. It was found that the diffraction efficiency is maintained when the temperature changes from room temperature (25 °C) to 60 °C. Figure S5 (Supporting Information) shows how the performance of the switchable Dammann grating changes when the temperature is increased. These results indicate that laser written LC devices can be used to create high-quality switchable Dammann gratings with high diffraction efficiency and relatively uniform intensity distribution across the spots in the array. In the future, further mixture refinement may enable improvements in the response times and the pattern quality, as well as preventing potential unwanted photocuring after the fabrication process. The nonreacted reactive mesogens have no influence on the actual performance of the device, provided that the devices are not exposed to blue/UV light post fabrication. Going forward, one approach would be to tailor the concentration of reactive mesogen to better suit the size/structure of the polymer network that needs to be formed, which will reduce the amount of nonreacted reactive mesogen after the gratings have been fabricated.

Figure 5 demonstrates the ability of the 2D switchable Dammann grating to work at a range of different wavelengths. By adjusting the voltage applied to the LC device according to the transmission-voltage curve for the sample, a phase difference of π can be achieved between the locked-in regions and nonlaser written regions. Figure 5a,b shows the off-state and on-state of the Dammann grating when illuminated with light of a wavelength of 520 nm. The images were captured using a CCD camera. The test voltage applied to the cell to control the director orientation of the nonlaser written regions

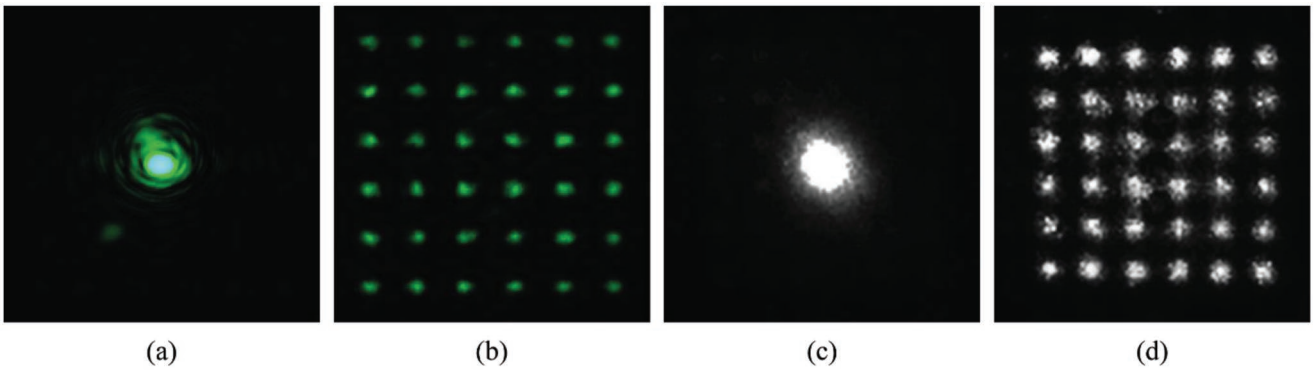

Figure 5. Demonstration of a switchable laser written LC Dammann Grating operating at two other wavelengths (λ = 520 nm and λ = 780 nm) by adjusting the voltage applied to the LC device. a) The replay field pattern for the voltage off-state at $V = 0$ V_{rms} for an incident wavelength of 520 nm captured with a CCD camera. b) The replay field pattern for the voltage on-state at $V = 1.14$ V_{rms} at a wavelength of 520 nm. c) The replay field pattern for the voltage off-state at $V = 0$ V_{rms} at a wavelength of 780 nm captured with a monochromatic CCD camera. d) The replay field pattern for the voltage on-state at $V = 1.54$ V_{rms} at a wavelength of 780 nm.

was $V = 1.14$ V_{rms}. Figure 5c,d, on the other hand, shows the switching of the Dammann grating when the LC device was illuminated by light of a wavelength of 780 nm. The 780 nm images were captured using a monochromatic CCD camera with the infrared filter removed. The voltage applied to turn the grating on was $V = 1.54$ V_{rms}. Note that the concentric circles seen in Figure 3f are not present here as the planar optical elements (e.g., wave plates) in our imaging system have been removed.

5. Interchangeable 2D Dammann Gratings

Figure 6 shows an LC device that consists of two separate Dammann gratings that give rise to different arrays of spots in the replay field. In this case, the sizes of the two gratings are both 1024 pixels × 1024 pixels, where each pixel was fabricated using the DLW to illuminate regions of 1 × 1 1 µm spots, which results in an overall grating size of 1024 µm × 1024 µm. The two Dammann gratings that were designed give rise to an array of 6 × 6 spots in a square configuration and 6 × 6 spots in a rhombus configuration. The gratings were fabricated in a glass cell with a thickness of 20 µm and were driven with a 1 kHz square wave with different voltage amplitudes during the fabrication process. The Dammann grating corresponding to the 6 × 6 rhombus pattern (pattern A) was fabricated in the presence of a voltage $V_A = 3.38$ V_{rms} applied to the LC cell. The Dammann grating corresponding to the 6 × 6 square pattern (pattern B) was fabricated when the LC cell was subjected to a voltage of $V_B = 5.96$ V_{rms}. Figure S6 (Supporting Information) illustrates the concept of an interchangeable Dammann grating fabricated using two-photon polymerization direct laser writing. The depths of the patterns fabricated within the LC layer were carefully chosen to ensure that they were close to the glass substrates and that they did not overlap with each other. These voltages were selected based on measurements of the transmission-voltage curve for the LC sample, which creates a π phase difference between the two laser-written gratings. It can be seen in Figure 6a,e that the Dammann gratings compare well with the design pattern (shown in the inset of each image). The diffraction patterns were obtained by applying the voltage that was used to write the other grating, i.e., applying voltage V_A (voltage for rhombus pattern fabrication) to observe pattern B (square pattern) in the replay field whereas applying V_B (voltage for square pattern fabrication) meant that pattern A (rhombus pattern) could be seen in the replay field. The phase only information from the pattern is highlighted in Figure 6b,f which was captured from POM with no analyzer installed.

The results for the 6 × 6 square diffraction pattern captured in the far field (replay field) in the replay system as well as the corresponding simulation results (shown in the insets) using the designed pattern are presented in Figure 6c. The square pattern results clearly illustrate the uniformity of the diffraction intensity distribution among all the spots as well as the high diffraction efficiency of the grating. Moreover, the results for the 6 × 6 rhombus diffraction pattern captured with two diagonals aligned with the camera are presented in Figure 6g. The corresponding simulation results using the designed pattern where the 2D pattern was generated by XOR-ing two 1D gratings with one of them being rotated by 30°, instead of 90°, are shown in the insets. The rhombus pattern results clearly illustrate the uniformity of the diffraction intensity distribution with irregular pattern design as well as the high diffraction efficiency of the spot generation. Figure 6d,h are the corresponding normalized intensity profiles for the array of spots recorded in the replay field. The results demonstrate that the fabricated bi-element grating configuration can switch readily between the two gratings by changing the voltage amplitude.

The square array of diffraction spots is distributed as designed with a uniform intensity distribution when the target voltage $V_A = 3.38$ V_{rms} was applied to the cell and completely changed to a rhombus pattern when a different voltage $V_B = 5.96$ V_{rms} was applied. The pattern designed to generate a 6 × 6 rhombus pattern in the far-field consisted of more quantized errors due to discrepancies between the theoretical transition points and the real fabricated pixels, which are caused by the non-90° rotation of the grating during the pattern design process. These discrepancies, along with fabrication errors, result in as much as a 20% deviation in the intensity across the elements in the far-field diffraction pattern. This nonuniformity in the intensity can be reduced through further

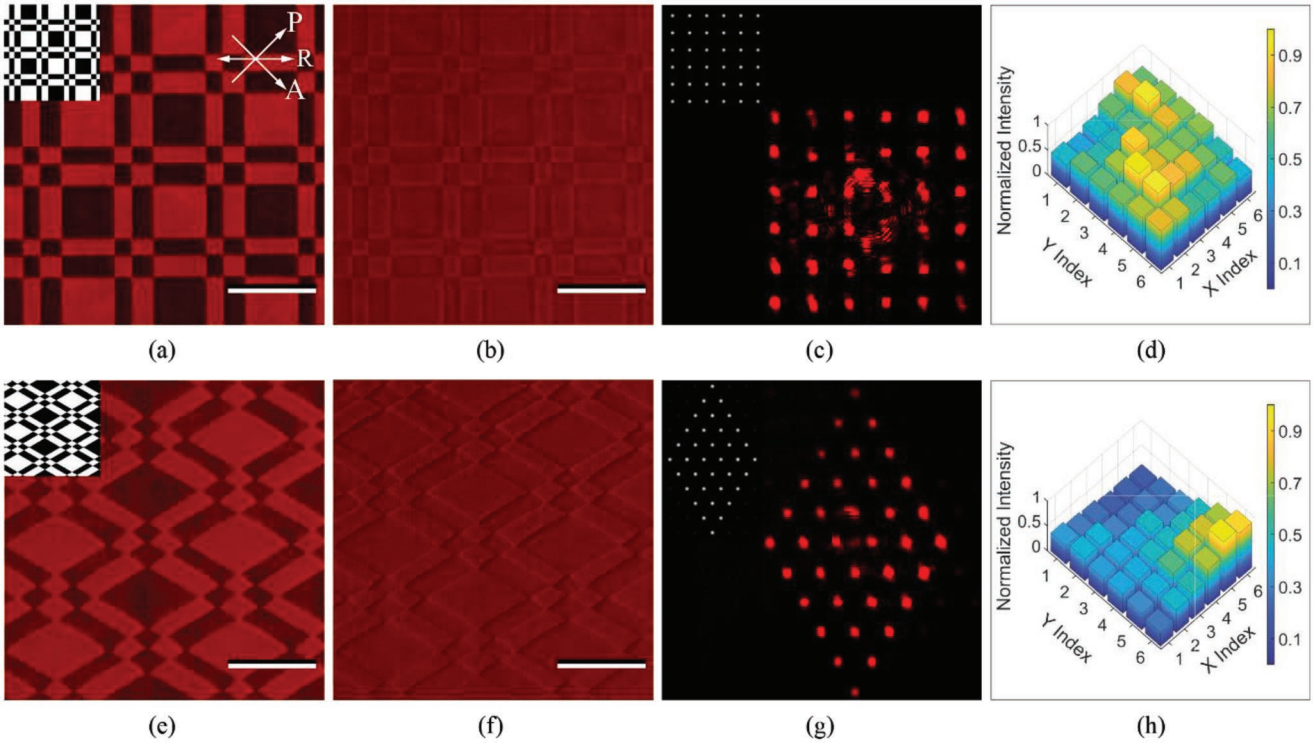

Figure 6. Demonstration of LC devices with interchangeable Dammann gratings. a) Microscope image of the Dammann grating that gives rise to a 6×6 square array in the replay field (with the grating design shown in the top left corner) fabricated at $V_A = 3.38\ V_{rms}$. The scale bar indicates 120 µm. The arrows indicate the direction of polarizer (P), analyser (A), and cell surface alignment direction (R). b) Phase only microscope image of the Dammann grating that gives rise to a 6×6 square array in the replay field fabricated at $V_A = 3.38\ V_{rms}$. The scale bar indicates 120 µm. c) Corresponding replay field pattern for the Dammann grating that generates a 6×6 square array in the replay field (with simulated replay field shown in the top left corner of the image). d) Corresponding bar chart showing the normalized intensity distribution in the 6×6 square array replay image. e) Microscope image of the Dammann grating that gives rise to a 6×6 rhombus array of spots in the replay field (with the grating design shown in the top left corner) fabricated at $V_B = 5.96\ V_{rms}$. The scale bar indicates 120 µm. f) Phase only microscope image of the Dammann grating that gives rise to a 6×6 rhombus array of spots in the replay fabricated at $V_B = 5.96\ V_{rms}$. The scale bar indicates 120 µm. g) Corresponding replay field pattern showing the 6×6 rhombus array of spots (the simulated replay field is shown in the top left corner). h) Corresponding bar chart showing the normalized distribution of intensity across the array of spots in the replay field.

refinements to the fabrication and design process. When the voltage applied was neither 3.38 V_{rms} nor 0.96 V_{rms}, which are the designed replay voltages in this case, the diffraction pattern will no longer be either a uniform 6×6 square beamlet array or a uniform 6×6 rhombus beamlet array. Instead, the 0th order spot dominates in the replay field with two lower intensity and overlapping square and rhombus beamlet arrays. When the designed voltages were applied to the device, the diffraction efficiency, which is defined as the ratio between the summation of the intensity of all diffraction spots and the nondiffracted initial laser spot, can reach ≈40%. The diffraction efficiency of the bi-element grating is lower than that of the single element grating and is believed to be due to the thicker LC layer as well as the presence of the other Dammann grating, which is not perfectly deactivated giving rise to more light scattering and loss. In order to improve the uniformity of the intensity in the diffraction pattern for interchangeable gratings, the fabrication process could be refined by rotating the sample between the fabrication on each substrate so that the pattern is along the scan direction. Furthermore, in future, the quantization errors can be incorporated into machine code generation when considering the design transition point values.

To analyze the fabrication quality in more detail, the cross-sections of one grating period of the square pattern were extracted from the microscope image and are summarized in **Table 1**. The normalized grayscale of the images was binarized at a threshold defined as the middle region between the maximum and minimum values. The actual transition points were then derived from the binarized values. Comparing the actual transition points derived from the cross section with the deigned transition points, it is found that the fabrication has led to a deviation in the transition points of less than 2% in

Table 1. Comparison between designed transition points and actual fabricated transition points for 6×6 patterns.

Transition points	ξ_1	ξ_2	ξ_3	ξ_4	ξ_5
Designed values	0.11444	0.20897	0.50000	0.61444	0.70897
Switchable pattern	0.10256	0.21927	0.50398	0.59863	0.71264
Interchangeable pattern—square	0.09328	0.21016	0.49859	0.59520	0.71227
Interchangeable pattern—rhombus	0.09180	0.21093	0.49965	0.59425	0.71268

accordance with that observed for the single element grating. In this case, the rise and fall response times recorded for the switchable pattern were found to be of the order of 120 ms and 900 ms, respectively, which did not vary significantly from the response times recorded from the nonpolymerized regions in the same device.

As the response time is known to be proportional to the square of the device thickness,[37] it is therefore reasonable that the 20 µm device exhibits a longer response time compared with that observed for the 5 µm device. Furthermore, because only two thin layers of LC close to the substrates have been polymerized by the laser writing process, there is still a large bulk of the LC that is free of a polymer network in the middle of the cell. This is unlike the situation in the 5 µm cell, where the polymerized network extended throughout the entire thickness of the LC layer. Thus, the two types of regions (polymerized and nonpolymerized) for the bi-element device have a similar response time.

6. Conclusions

In conclusion, in this paper we have demonstrated a bi-element LC Dammann grating that can be switched between different gratings, and thus different patterns in the replay field, with the application of a voltage. A series of simulations have been carried out to verify the design of the Dammann grating, predict the far-field diffraction pattern and determine the fabrication parameters required to achieve high quality gratings with good intensity uniformity across the elements in the array. These simulation results are further verified with the use of a spatial light modulator. A single element switchable grating is first fabricated and characterized to prove that the parameters derived from the simulations are suitable for fabrication. It is also demonstrated that the single element switchable grating can function across a range of wavelengths by simply varying the voltage to always ensure a phase difference of π between the laser written and nonlaser written regions of the grating. Following this, a more sophisticated bi-element grating structure was designed and fabricated in an LC layer whereby the far-field pattern switches between a square array and a rhombus array with the application of a voltage. Analysis of the fabrication transition points as well as the response time highlights the high fabrication quality of these laser-written LC Dammann gratings that could be of importance for a range of applications such as optical communications, optical computing, and laser beam shaping. In future work, it would be highly desirable if the Dammann gratings could also be erasable and rewritten, which could potentially increase the applicability of these diffractive optic elements. One way that this might be achieved is if the polymer network could be erased and reformed using two different illumination wavelengths.

7. Experimental Section

Mixture Preparation Process: The polymerizable mixture used for this experiment contains 30 wt% of the reactive mesogen RM257 and 1 wt% of the photoinitiator Irgacure 819, with the rest being the nematic LC mixture E7 (69 wt%). The mixture was heated up to the isotropic phase before it was capillary filled into a glass cell made up of two indium tin oxide (ITO) coated glass slides whose gap in between was precisely controlled by 5 µm (or 20 µm for interchangeable 2D Dammann gratings) spacer beads spread throughout the whole region of the cell. The surface of the cell, which was manufactured by Instec, was coated with polyimide and rubbed antiparallel with a pre-tilt of 2–3°. The LC device was then cooled down to room temperature and mounted on a custom built TPP-DLW system for fabrication. A function generator (Multicomp MP750510) with an amplifier (FLC Electronics F10AD) having a fixed amplification factor of 10 was also connected to vary the field applied to the cell during the fabrication.

Two-Photon Polymerization Direct Laser Writing System: A schematic of the TPP-DLW system is illustrated in Figure S7 (Supporting Information). The laser source was a mode-locked Titanium-Sapphire femtosecond laser (Spectra-Physics Tsunami) at 780 nm, which was pumped by a diode-pumped solid state (DPSS) CW laser (Spectra-Physics Millennia V) at 532 nm, emitting 100 fs pulses at a repetition rate of 80 MHz. The laser was focused into the LC layer of the cell using an Olympus 0.45 NA objective lens. The power of the fabrication laser focused into the LC layer after the objective was 40 mW. The voltage-controlled sample is mounted onto a 3D printed adapter on a 3-axis piezo translational stage with positioning resolution of 1nm and movement accuracy of 100 nm (Aerotech ANT95XY-050 and ANT95V-3). The halogen bulb beside the stage illuminates the sample with an orange (550 nm) filter so that the photocuring process could be monitored with an in-situ monochrome CCD camera in real time. A polarized optical microscope configuration was setup by forming an image of the illuminated sample through the dichroic mirror before it was captured by a CCD camera using a lens of 200 mm focal length with a polarizer and analyzer installed. The LC mixture was polymerized by moving the device under the focus of the pulsed laser beam at a speed of 0.1 mm/s. The LC device was driven by a 1 kHz square wave of voltage ranging between 0 V_{rms} and 10 V_{rms}.

Polarized Optical Microscopy: Polarizing optical microscope images were captured using a QImaging Retiga R6 camera mounted onto the phototube of an Olympus BX51 optical microscope. Olympus objective lenses were used where the cover slip correction collar was set to the thickness of the glass slides of the LC device, in order to improve the quality of the images by reducing aberrations. A filter at a wavelength of 660 nm with 10 nm bandwidth was installed in front of the halogen bulb of the microscope to prevent the sample from post-curing during observation. The analyzer and polarizer in the microscope were set to be crossed and the sample was rotated until the brightest state was located.

Dammann Grating Design Test on the SLM: The SLM consists of a grid of nematic LC pixels which have a linear switching range between 0 and 2π at a wavelength of 780 nm. A Dammann grating was loaded onto the SLM, which was installed in an off-axis replay configuration. This characterization system is illustrated in Figure S8 (Supporting Information). The laser had a wavelength of $\lambda = 780$ nm. The power of the laser was attenuated using a neutral density (ND) filter of optical density (OD) of OD = 0.2. A 4f beam expanding system was also included with $f_1 = 25.4$ mm and $f_2 = 125$ mm, which resulted in an expansion of the beam to suit the size of the effective area of the SLM. The replay images were then captured by a CCD after a lens on an off-axis position. By loading the designed Dammann grating pattern on to the SLM, the far field image could then be captured by a CCD camera.

Replay Field Images: A schematic of the replay field imaging system is illustrated in Figure S9 (Supporting Information), which contains several subsystems. The available laser sources were Thorlabs compact laser modules with wavelengths of 635 nm and 520 nm as well as an Edmund Optics compact laser module with wavelength of 780 nm. Figure S9 (Supporting Information) demonstrates the setup with the 635 nm laser source. The intensity of the laser was controlled by a circular, continuously variable reflective ND filter. It was composed of a UV fused silica glass substrate and a metallic Inconel coating through a full 270°, ensuring a flat spectral response from the ultraviolet to the mid-infrared. The laser beam after the ND filter then passed through the beam polarization control subsystem, which is made up of a polarizer and a half-wave plate. The polarizer was mounted onto a rotary mount to alter

the polarization state of the laser. After the reflection between a pair of mirrors, the beam entered the half-wave plate. The half-wave plate was mounted on a manual rotating stage to vary the polarization state of the incident ray onto the LC device. To illuminate only the grating, the beam size had to be reduced from its original size. So, after the polarization conditioning optics, the beam was then shrunk by a pair of lenses L1 and L2 whose focal lengths were 125 and 25.4 mm, respectively. Then the far field images were captured using the CCD or a digital SLR camera either directly or from the screen mounted at the far end.

Supporting Information

Supporting Information is available from the Wiley Online Library or from the author.

Acknowledgements

P.S. gratefully acknowledges the Engineering and Physical Sciences Research Council (UK) for a Fellowship (EP/R004803/01). The authors also gratefully acknowledge The Royal Society and The John Fell Fund (Oxford) for financial support.

Conflict of Interest

The authors declare no conflict of interest.

Data Availability Statement

The data that support the findings of this study are openly available in Oxford University Research Archive at 10.5287/bodleian:dmZdEGqKD, reference number 477613.

Keywords

Dammann gratings, two-photon polymerization, laser writing, liquid crystals, reactive mesogens

Received: May 30, 2022
Revised: July 15, 2022
Published online: October 6, 2022

[1] H. Dammann, K. Görtler, *Opt. Commun.* **1971**, *3*, 312.
[2] H. Dammann, E. Klotz, *Opt. Acta* **1977**, *24*, 505.
[3] U. Killat, G. Rabe, W. Rave, *Fiber Integr. Opt.* **1982**, *4*, 159.
[4] J. Jahns, M. M. Downs, M. E. Prise, N. Streibi, S. J. Walker, *Opt. Eng.* **1989**, *28*, 281267.
[5] J. N. Mait, *Opt. Lett.* **1989**, *14*, 196.
[6] U. Krackhardt, N. Streibl, *Opt. Commun.* **1989**, *74*, 31.
[7] J. A. Davis, J. Guertin, D. M. Cottrell, *Appl. Opt.* **1993**, *32*, 6368.
[8] S. Franssila, *Introduction to Microfabrication*, John Wiley & Sons, Chichester, West Sussex, UK **2010**.
[9] M. Deubel, G. von Freymann, M. Wegener, S. Pereira, K. Busch, C. M. Soukoulis, *Nat. Mater.* **2004**, *3*, 444.
[10] N. Anscombe, *Nat. Photonics* **2010**, *4*, 22.
[11] T. Gissibl, S. Thiele, A. Herkommer, H. Giessen, *Nat. Photonics* **2016**, *10*, 554.
[12] I. Moreno, J. A. Davis, D. M. Cottrell, N. Zhang, X.-C. Yuan, *Opt. Lett.* **2010**, *35*, 1536.
[13] P. García-Martínez, M. M. Sánchez-López, J. A. Davis, D. M. Cottrell, D. Sand, I. Moreno, *Appl. Opt.* **2012**, *51*, 1375.
[14] Z. Ye, W. Liu, Sun, G. Jin, J. Li, Y. Xie, C. Zhou, W. Jia, *Microwave Opt. Technol. Lett.* **2021**, *63*, 2297.
[15] Z.-N. Yuan, Z.-B. Sun, H.-S. Kwok, A. K. Srivastava, *Liq. Cryst.* **2021**, *48*, 1402.
[16] R. L. Morrison, *J. Opt. Soc. Am. A* **1992**, *9*, 464.
[17] A. Vasara, M. R. Taghizadeh, J. Turunen, J. Westerholm, E. Noponen, H. Ichikawa, J. M. Miller, T. Jaakkola, S. Kuisma, *Appl. Opt.* **1992**, *31*, 3320.
[18] C. Zhou, L. Liu, *Appl. Opt.* **1995**, *34*, 5961.
[19] C. Zhou, J. Jia, L. Liu, *Opt. Lett.* **2003**, *28*, 2174.
[20] J. Yu, C. Zhou, W. Jia, W. Cao, S. Wang, J. Ma, H. Cao, *Appl. Opt.* **2012**, *51*, 1619.
[21] A. Dickinson, M. E. Prise, *Appl. Opt.* **1990**, *29*, 2001.
[22] C. Xiang, J. Wang, Y. Xie, D. Zhao, W. Jia, C. Zhou, *Proc. SPIE* **2018**, *10818*, 201.
[23] C. Zhao, F. Fan, A. Tam, M. Schadt, V. Chigrinov, H.-S. Kwok, *SID Symp. Digest Tech. Pap.* **2018**, *49*, 1718.
[24] H. Pang, A. Cao, W. Liu, L. Shi, Q. Deng, *IEEE Photonics J.* **2019**, *11*, 1.
[25] K. Liu, C. Zhou, S. Wei, S. Wang, S. Li, Y. Li, J. Wang, Y. Lu, *Proc. SPIE* **2014**, *9271*, 85.
[26] S.-J. Ge, Chen, L.-L. Ma, Z. Liu, Z.-G. Zheng, D. Shen, W. Hu, Y.-Q. Lu, *Opt. Mater. Express* **2016**, *6*, 1087.
[27] F. Fan, L. Yao, X. Wang, L. Shi, A. Srivastava, V. Chigrinov, H.-S. Kwok, S. Wen, *Crystals* **2017**, *7*, 79.
[28] Z. He, K. Yin, K.-H. Fan-Chiang, S.-T. Wu, *Crystals* **2021**, *11*, 195.
[29] X.-Q. Wang, A. K. Srivastava, F. Fan, Z.-g. Zheng, D. Shen, V. G. Chigrinov, H.-S. Kwok, *Opt. Lett.* **2016**, *41*, 5668.
[30] Z.-N. Yuan, Z. Sun, H.-S. Kwok, A. K. Srivastava, *SID Symp. Digest Tech. Pap.* **2020**, *51*, 769.
[31] V. Chigrinov, A. Muravski, H. S. Kwok, H. Takada, H. Akiyama, H. Takatsu, *Phys. Rev. E* **2003**, *68*, 061702.
[32] Y. Shi, P. S. Salter, M. Li, R. A. Taylor, S. J. Elston, S. M. Morris, D. D. C. Bradley, *Adv. Funct. Mater.* **2020**, *31*, 2007493.
[33] C. C. Tartan, P. S. Salter, T. D. Wilkinson, M. J. Booth, S. M. Morris, S. J. Elston, *RSC Adv.* **2017**, *7*, 507.
[34] C. C. Tartan, J. J. S. O'Neill, P. S. Salter, J. Aplinc, M. J. Booth, M. Ravnik, S. M. Morris, S. J. Elston, *Adv. Opt. Mater.* **2018**, *6*, 1800515.
[35] J. J. S. O'Neill, P. S. Salter, M. J. Booth, S. J. Elston, S. M. Morris, *Nat. Commun.* **2020**, *11*, 2203.
[36] J. S. O'Neill, P. S. Salter, Z. Zhao, B. Chen, H. Daginawalla, M. J. Booth, S. J. Elston, S. M. Morris, *Adv. Opt. Mater.* **2022**, *10*, 2102446.
[37] I. W. Stewart, *The Static and Dynamic Continuum Theory of Liquid Crystals*, CRC Press, Boca Raton, FL **2019**.
[38] K. K. Vardanyan, J. Qi, J. N. Eakin, M. D. Sarkar, G. P. Crawford, *Appl. Phys. Lett.* **2002**, *81*, 4736.
[39] H. Shim, H.-K. Lyu, B. Allabergenov, Y. Garbovskiy, A. Glushchenko, B. Choi, *Liq. Cryst.* **2016**, *43*, 1390.